Drift-diffusion modeling of photocurrent transients in bulk heterojunction solar cells

Inchan Hwang, Christopher R. McNeill, and Neil C. Greenham[a)]
Department of Physics, Cavendish Laboratory, University of Cambridge, J. J. Thomson Ave.,
Cambridge CB3 0HE, United Kingdom

We utilize a time-dependent drift-diffusion model incorporating electron trapping and field-dependent charge separation to explore the device physics of organic bulk-heterojunction solar cells based on blends of poly(3-hexylthiophene) (P3HT) with a red polyfluorene copolymer. The model is used to reproduce experimental photocurrent transients measured in response to a step-function excitation of light of varied intensity. The experimental photocurrent transients are characterized by (i) a fast rise of order 1 μs followed by (ii) a slow rise of order 10–100 μs that evolves into a transient peak at high intensity, (iii) a fast decay component after turn-off and (iv) a long-lived tail with magnitude that does not scale linearly with light intensity or steady-state photocurrent. The fast rise and decay components are explained by the transport of mobile carriers while the slow rise and decay components are explained by slower electron trapping and detrapping processes. The transient photocurrent peak at high intensities with subsequent decay to the steady-state value is explained by trap-mediated space-charge effects. The build-up of trapped electrons in the device produces reduction in the strength of the electric field near the transparent anode that increases the likelihood of bimolecular recombination, and lowers the overall efficiency of charge dissociation in the device. Notably the model demonstrates that a reduction in free charge generation rate by space-charge effects is as significant as bimolecular recombination in this device assuming Langevin-type bimolecular recombination. The model is also used to explore the dynamics of charge separation with an upper bound of 50 ns set for the lifetime of electron-hole pairs, and to provide an estimate of the trap density of 1.3×10^{22} m^{-3}. © *2009 American Institute of Physics*. [doi:10.1063/1.3247547]

I. INTRODUCTION

Bulk heterojunction organic solar cells are an interesting class of device and a potential route to low-cost photovoltaic technology.[1] Such devices consist of a blended film of two semiconductors with high interfacial area facilitating charge generation (exciton dissociation) yet with separated, interconnected networks for efficient charge collection. Efficient device operation has been demonstrated using various combinations of semiconductors including conjugated polymer/fullerene blends,[2,3] polymer/polymer blends,[4] and polymer/nanocrystal blends.[5] A key process in the operation of these devices is the separation of bound charges (polaron pairs) from the donor/acceptor interface following exciton dissociation that is often described as an Onsager–Braun-type process.[6] In particular under low light intensities the different efficiencies of these devices may be explained solely by differences in the efficiency of this charge separation process.[7]

At higher light intensities, particularly under solar illumination, device operation becomes more complicated with an accumulation of charge in the device that affects the internal electric field distribution and increases the occurrence of bimolecular recombination. In order to understand the complex behavior of these devices under higher light intensities, more sophisticated experimental and analytical approaches are required. A range of new experimental approaches have been developed recently to study the device physics and recombination dynamics in organic solar cells by subjecting organic solar cells to an electrical or optical perturbation (or sometimes both). Examples of such techniques include the carrier extraction by linearly increasing voltage (CELIV) (Ref. 8) and photo-CELIV techniques,[9] the time-of-flight (TOF) technique,[10,11] the double injection technique,[11,12] and flash-photolysis time-resolved microwave photoconductivity.[13] Recently we have studied the response of efficient all-polymer solar cells to a step function of optical excitation as a function of light intensity. Pulse widths of 500 ns and 100 μs were employed to study the fast turn-on and turn-off dynamics of free charges, as well as slower dynamics that were attributed to the processes of charge trapping and detrapping.[14] In particular, it was shown that the time scale over which dynamics of an organic cell are investigated should extend to the time taken for the device to reach equilibrium in order to fully capture the behavior of the device. In order to aid interpretation of the photocurrent transients observed, we have also developed a time-dependent drift-diffusion model.[15] This model incorporates many features of the successful drift-diffusion model developed by Blom and co-workers[6,16] to explain the steady-state operation of organic bulk heterojunction solar cells such as the use of the effective medium approach and incorporation of an Onsager–Braun charge separation term. In our previous

experimental paper we briefly presented results of the numerical model that reproduced the experimental results, justifying our interpretation of the origin of the transient features observed. Here we present the full detail of our model including discussion of the various parameters used and extended discussion on the device physics revealed by this combined experimental/modeling approach.

II. EXPERIMENT

The bulk heterojunction devices used in this study were based on blends of poly(3-hexylthiophene) (P3HT) with the red polyfluorene derivative poly((9,9-dioctylfluorene)-2,7-diyl-alt-[4,7-bis(3-hexylthien-5-yl)-2,1,3-benzothiadiazole]-2′,2″-diyl) (F8TBT).[17] This polymer combination has shown promise as devices made of these materials demonstrate one of the highest efficiencies for all-polymer blends. In this configuration, P3HT acts as an electron donor and F8TBT acts as an electron acceptor.[17] Full experimental details can be found in our previous publication.[14] Briefly, devices were fabricated with a glass (1 mm)/indium-tin-oxide (ITO) (140 nm)/poly(3,4-ethylenedioxythiophene):polystyrene sulfonic acid (PEDOT:PSS) (40 nm)/P3HT:F8TBT blend (220 nm, 1:1 weight ratio)/Al (100 nm) architecture. Devices were fabricated and encapsulated in a nitrogen glovebox, and annealed after cathode deposition at 140 °C for 10 min to optimize device performance.[18] Pulse measurements were performed using a 500 ns or a 100 μs square pulse of light generated using a pulse generator (Hewlett Packard 8116A) connected to a high intensity InGaN light-emitting diode (peak emission wavelength of 525 nm, 35 nm half-width). The rise/fall time of the light was measured to be less than 50 ns by a New Focus 1621 nanosecond silicon photodetector. Photocurrent was measured using the 50 Ω input impedance of a Hewlett Packard 54502A digitizing oscilloscope. Intensity was varied using a neutral density wheel calibrated with a Hamamatsu S8746-01 calibrated silicon photodiode. Figure 1 presents the typical photocurrent transients observed in a device with 220 nm thick active layer in response to 100 μs square pulses of light of various intensities. At low intensity, after turn-on the device demonstrates an initial, fast rise followed by a slower increase with the device taking ~100 μs to reach equilibrium. Similarly, after turn-off a sharp decrease in the photocurrent is observed followed by a longer photocurrent tail with charge still being extracted after 500 μs as revealed on a logarithmic scale. However, at high intensity, a more complicated turn-on behavior is observed with a peak in the transient photocurrent observed before a decay in photocurrent to the steady-state photocurrent level. A long photocurrent tail with similar kinetics is also observed after turn-off at high intensity, however the amount of charge extracted after turn-off scales sublinearly with the steady-state photocurrent after turn-on. These effects have been attributed to the influence of charge trapping in the device with the long tail after turn-off arising due to the slow detrapping of charge after turn-off and after the mobile carriers have been swept out of the device. Furthermore, the transient peak observed after turn-on at high intensity has been attributed to a trap-mediated build-up of charge in the
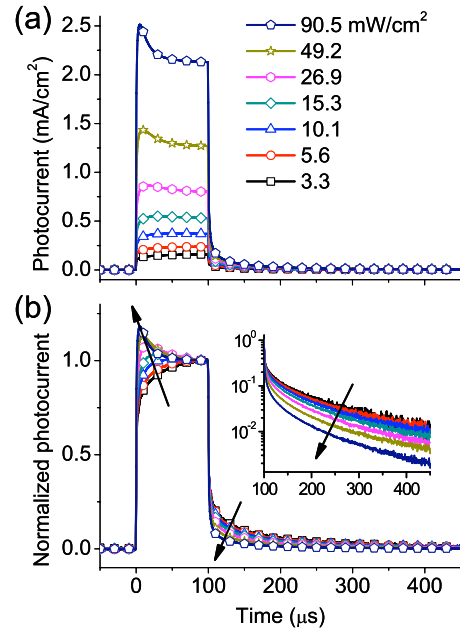

FIG. 1. (Color online) (a) Unnormalized and (b) normalized photocurrent transients measured in a 220 nm thick P3HT:F8TBT blend solar cell given a 100 μs square pulse of light with variable intensity at short circuit. The inset represents the normalized data on a logarithmic current scale.

device that redistributes the internal electric field in the device, with the field becoming higher near the cathode (in an attempt to sweep out the excess negative charge) and lower near the anode (that increases the population of holes balancing the excess negative charge in the device). The result of this electric field redistribution is twofold. First, the build-up of holes near the anode causes a significant overlap in the electron and hole densities that may promote bimolecular recombination. Second, since the optical field (and hence the charge pair generation rate) is highest near the anode, the reduction in the electric field strength near the anode may result in a reduction in charge generation efficiency due to the electric-field dependent charge dissociation rate. The fact that charge trapping and detrapping occur on a longer time scale than the transport of free charge accounts for the two components (fast and slow) of the rise and fall.

III. NUMERICAL METHODS

We now detail the numerical approach used to reproduce the experimental photocurrent transients of Fig. 1. This model is an extension of our purely theoretical treatment published previously[15] using the one-dimensional drift-diffusion equations[15] with the z direction denoting the direction perpendicular to the plane of the device. For simplicity, the internal nanostructure of the active layer is ignored, and it is assumed that the device can be modeled by an effective medium approach[16] with electron and hole mobilities μ_n and μ_p representing the transport of the respective carrier through the acceptor (F8TBT) or donor (P3HT) component of the blend. In addition to the equations used previously,[15] we also include a Poole–Frenkel expression to describe the transport of charge, and we separate the total density of elec-

TABLE I. The parameters used for fitting in Figs. 3 and 6 and partially used for the other figures.

Parameter	Symbol	Numerical value
Refractive index at 525 nm	n	1.75
Extinction coefficient at 525 nm	k	0.49
Electron zero-field mobility	μ_{n0}	9.9×10^{-4} cm^2 V^{-1} s^{-1}
Hole zero-field mobility	μ_{p0}	1.8×10^{-4} cm^2 V^{-1} s^{-1}
Field-dependence parameter for electron	γ_n	1.5×10^{-5} (V/m)$^{-1/2}$
Field-dependence parameter for hole	γ_p	-2.2×10^{-4} (V/m)$^{-1/2}$
Geminate charge pair distance	a	2.8 nm
Geminate recombination rate constant	k_{rec}	1.3×10^7 s^{-1}
Density of trap sites	N_t	1.3×10^{22} m^{-3}
Trapping rate constant	C_t	2.5×10^{-16} m^3 s^{-1}
Detrapping rate constant	C_{dt}	1.0×10^4 s^{-1}
Temperature	T	300 K
Relative permittivity	ε_r	3
Voltage under short circuit conditions	V	-0.9 V
Thickness	d	220 nm
Charge pair generation rate for unit light intensity	$(G_0)_{max}$	1.63×10^{26} m^{-3} s^{-1}

trons n into "free", n_f, and trapped, n_t, electron densities. Denoting hole and charge-pair densities by p and X, respectively, the relevant equations are

$$\frac{\partial n_f}{\partial t} = \frac{1}{e}\frac{\partial}{\partial z}\left[\mu_n k_B T\frac{\partial n_f}{\partial z} + \mu_n n_f eE\right] + (k_{diss}X - \gamma n_f p)$$
$$- \frac{\partial n_t}{\partial t}, \tag{1}$$

$$\frac{\partial n_t}{\partial t} = C_t(N_t - n_t)n_f - C_{dt}n_t, \tag{2}$$

$$\frac{\partial p}{\partial t} = \frac{1}{e}\frac{\partial}{\partial z}\left[\mu_p k_B T\frac{\partial p}{\partial z} - \mu_p peE\right] + (k_{diss}X - \gamma n_f p), \tag{3}$$

$$\mu_{n(p)} = \mu_{n0(p0)}\exp(\gamma_{n(p)}\sqrt{|E|}), \tag{4}$$

$$n = n_f + n_t, \tag{5}$$

$$\frac{\partial E}{\partial z} = \frac{e(p-n)}{\varepsilon_0\varepsilon_r}, \tag{6}$$

$$\frac{\partial X}{\partial t} = IG_0(z) - k_{rec}X - k_{diss}(z,E,T)X + \gamma n_f p, \tag{7}$$

$$k_{diss}(z,T,E) = \frac{3\gamma}{4\pi a^3}\exp\left(-\frac{E_B}{k_B T}\right)\frac{J_1(2\sqrt{-2b})}{\sqrt{-2b}}, \tag{8}$$

where e is the elementary charge, E is the electric field, ε_0 is the permittivity of free space and ε_r is the relative permittivity of the polymer, t is the time, T is the absolute temperature, k_B is Boltzmann's constant, E_B is the binding energy of charge pairs, and $b=e^3|E|/(8\pi\varepsilon_0\varepsilon_r k_B^2 T^2)$. Equations (1) and (3) represent the coupled drift-diffusion equations for free electrons and holes with generation of free carriers by dissociation of charge pairs with rate constant k_{diss}, and bimolecular recombination of free electrons and holes to form charge pairs with Langevin recombination rate constant γ. Equation

(2) describes the dynamics of trapping and detrapping of free electrons into or from trap sites N_t with a trapping rate constant C_t and a detrapping rate constant C_{dt}. Equation (4) describes the Poole–Frenkel behavior of free charge carriers with μ_{n0} (μ_{p0}) denoting the zero-field mobility of electrons (holes) and γ_n (γ_p) as the field-dependence parameter for electrons (holes). The charge density dependence of mobility[19] is ignored for simplicity. Equation (6) represents the change in electric field E inside the device due to space charge. Equation (7) describes the dynamics of charge pairs which are created with rate IG_0 ($=G$), which is assumed to be linearly proportional to light intensity. I denotes intensity of light and G_0 represents the generation rate of charge pairs created at unit light intensity.

Equation (2) incorporates an electron trapping term coupled with Eq. (1). Previous experimental results have provided clear evidence for the trapping of electrons in the blend rather than holes, although the precise mechanism for electron trapping is unclear.[20] For simplicity, we have used a single trapping energy level [Eq. (2)] as used by Ginger and Greenham[21] for dark current simulations of CdSe nanoparticles, although multiple trapping energy levels are likely to be more appropriate,[22,23] but are computationally difficult and require additional fitting parameters

For boundary conditions we assume thermionic injection in the presence of image charge effects[24,25] with 0.5 eV barriers at each electrode. We fix the total voltage across the active layer to be 0.9 V as a built-in voltage, corresponding to the open-circuit voltage of the 220 nm thick device,[14] to simulate short-circuit conditions. The recombination rate constant γ is assumed to be of the Langevin form $e(\mu_n + \mu_p)/\varepsilon_0\varepsilon_r$, and the charge-pair dissociation is assumed to be Onsager-like,[6,26] with an initial pair separation of $a = 2.8$ nm. The device thickness is 220 nm, $\varepsilon_r=3$ and $T = 300$ K. All parameters used for fitting to Figs. 3 and 5 are summarized in Table I, and are used throughout the rest of this paper unless otherwise specified.

We solve the above equations numerically on a spatial grid dividing the 220 nm active layer into 71 points and
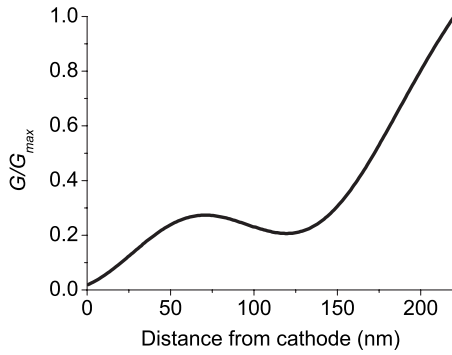
FIG. 2. The normalized charge pair generation rate profile that we have used in all modeling is shown. The excitation light wavelength is 525 nm. The origin corresponds to the cathode.

FIG. 3. (Color online) Fitting the numerical results (solid line) to the experimental results (-□-) in order to extract free charge mobilities, field dependence parameter and charge generation efficiency in short-pulse current transients. $a = 2.8$ nm ($k_{diss} = 3.33 \times 10^7$ s^{-1}), k_{rec} is 1.30×10^7 s^{-1} with a corresponding geminate charge-pair lifetime of 22 ns.

integrating forward in time. The initial conditions in the dark ($G = 0$) are found by starting with zero charge density and integrating forward until a steady state is reached. Then the illumination is turned on ($G \neq 0$) and the current

$$J = \left(\mu_n \frac{\partial n_f}{\partial z} - \mu_p \frac{\partial p}{\partial z} \right) k_B T + (\mu_n n_f + \mu_p p) e E, \qquad (9)$$

is recorded at each time step. Since we are considering non-steady-state conditions, the current is not required to be identical at each point in the device. To obtain the experimentally measured current in the external circuit, we average the current density throughout the device, thus accounting for both real and displacement currents.[6,27]

Finally, since light is not uniformly absorbed in the active layer of the device, an optical absorption profile is needed. Optical absorption in the active layer was modeled using the transfer matrix approach,[28] with the refractive index and extinction coefficient of the blend measured with a spectroscopic ellipsometer (VASE by Woollam, Inc.). In order to obtain the optical constants for annealed P3HT:F8TBT blends, a uniaxially anisotropic Cauchy dispersion model was first used to fit the reflection and transmission ellipsometry data in the transparent region. The normal-incidence transmission spectrum was then measured. To determine the in-plane (ordinary) optical constants in the absorbing region, a general oscillator model was used to fit to the transmission data using seven Gaussian oscillators, combined with the Cauchy dispersion. The chosen model ensures Kramers–Krönig consistency. We obtained optical constants for ITO, PEDOT, and aluminum from the literature.[29,30] Further details can be found in a previous publication.[31] Figure 2 presents the optical absorption profile modeled using this approach, showing that light is effectively attenuated in the device at the wavelength used due to the high extinction coefficient of the active layer at this wavelength. The profile of Fig. 2 has been employed in the numerical simulation as the charge pair generation rate profile $G(z)/G_{max}$.

IV. DISCUSSION

A. Fitting of short-pulse photocurrent transients

We now justify our choice of parameters listed in Table I and show how the choice of parameters influences the mod-
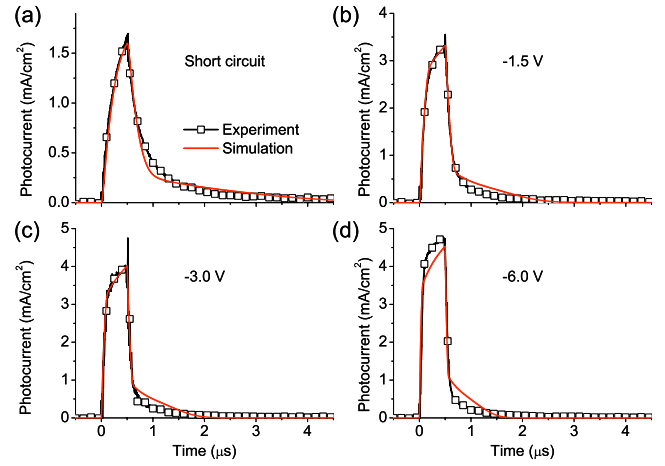
eled photocurrent transients. For simplicity, we first model the response of the device to a 500 ns square pulse of light, Fig. 3. The shape of these photocurrent transients is independent of the light intensity of the pulse and of a constant background source.[14] Furthermore, the shape and magnitude of the transient curves change with the applied electric field, providing strong evidence that they reflect the transport of free charge alone, with trapping and de-trapping phenomena occurring on a much longer time scale. Figure 3 shows the final results of fitting the numerical model to the photocurrent transients with different applied electric fields with the parameters listed in Table I. The fitting process was applied iteratively for the short-pulse photocurrent transients and the long-pulse photocurrent transients. Mobilities of free charge carriers (that largely determine the dynamics on this time scale) are obtained from the fit to the short-pulse photocurrent transients with trapping and detrapping initially disabled. Then the parameters determining trapping and detrapping processes are obtained by the fit to the long-pulse photocurrent transients, as described later, in Sec. IV B. Inclusion of trapping has a minor influence on the height of the photocurrent transients during the fast rise, requiring slight further optimization of the mobilities to obtain the fit shown in Fig. 3. Fitting the electric-field dependence of the fast photocurrent transients informs not only our choice of transport parameters but also our choice of charge generation parameters (a and k_{rec}) as will be discussed below. In general a good fit is obtained to the photocurrent rise with the two rise components (one faster and one slower) accounted for by two different mobilities, $\mu_{n0} = 9.9 \times 10^{-4}$ cm^2 V^{-1} s^{-1} and $\mu_{p0} = 1.8 \times 10^{-4}$ cm^2 V^{-1} s^{-1}. Somewhat surprisingly, an electron mobility that is higher than the hole mobility provides a better fit to this rise, however the effective mobility as measured by other techniques will be lower due to the effect of traps that are not seen in this measurement. We also note that a negative field dependence parameter γ_p is used for holes, which has been independently verified by TOF measurements[20] and is attributed to spatial disorder.[32] TOF mobilities of $\sim 8 \times 10^{-5}$ cm^2 V^{-1} s^{-1} are measured for holes
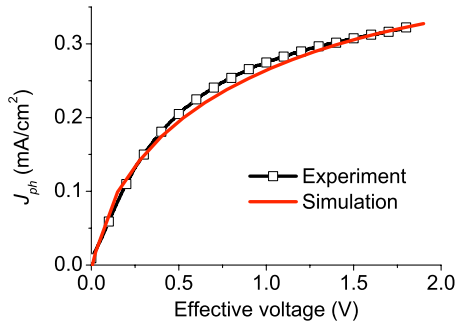
FIG. 4. (Color online) Photocurrent density plotted against effective voltage in experiment (-□-) and simulation (solid line), showing a good agreement with the parameters used in the Table I.

FIG. 5. (Color online) Photocurrent transients of experimental (-□-) and simulation (solid line and dashed line) in response to a 500 ns light pulse. In the simulation, the dissociation rate constant a (and hence k_{diss}) is varied. The geminate recombination rate k_{rec} is varied concomitantly with varying a in order to maintain the same charge generation efficiency. The other parameters remain constant as in the table. For $a=1.5$ nm ($k_{diss}=6.92\times10^5$ s^{-1}), k_{rec} is 2.69×10^5 s^{-1} with a charge pair lifetime of 1 μs leading to a time delay after turn-off. For $a=3.5$ nm ($k_{diss}=6.42\times10^7$ s^{-1}), k_{rec} is 2.50×10^7 s^{-1} with a charge pair lifetime of 11.2 ns, leading to no time delay.

at low fields which are close to the zero-field mobility used in the model. Electron mobilities measured by TOF (Ref. [20]) are lower than the zero-field electron mobility used to fit the 500 ns transients due to trapping effects as discussed above. The effective mobility due to the presence of traps is about two orders of magnitude lower (discussed below). The photocurrent tail is not as well fitted by the model, which may be due to the effects of dispersive transport which are not described by the model.

We now discuss the role of charge pair separation and recombination in our model. An important parameter here is the charge generation efficiency P, which in the Onsager–Braun model is given by

$$P = k_{diss}(E)/[k_{diss}(E) + k_{rec}] = [1 + k_{rec}/k_{diss}(E)]^{-1}. \quad (10)$$

At low intensities, this parameter should directly determine the short-circuit quantum efficiency and the shape of the current-voltage curve arises from the field dependence of k_{diss}. Although the field dependence of k_{diss} is determined solely by the dielectric constant [Eq. (9)], the strength of the field dependence of P is also influenced by the ratio $k_{rec}/k_{diss}(0)$. The steady-state current-voltage curve for our device is shown in Fig. 4, and corresponds to a short-circuit quantum efficiency of 0.17.[14] From optical modeling and photoluminescence quenching data it is clear that most incident photons produce charge pairs, and hence a significant fraction of these charge-pairs are not separated at short-circuit. However, choosing a value of k_{rec}/k_{diss} to reproduce the observed quantum efficiency does not allow the shape of the current-voltage curve to be reproduced. This indicates the existence of a separate population of charge pairs which are not dissociated under the fields relevant to these experiments, either because they have a significantly smaller initial charge-pair separation, or because they have a very rapid recombination channel. It is therefore probably appropriate to consider a distribution of initial charge-pair separations.[33] Furthermore, in a blend morphology, Monte Carlo simulations have shown that the effective medium approach is not valid[34,35] and that heterojunctions with unfavorable orientations with respect to the applied field will have their charge generation efficiency suppressed rather than enhanced by the field.[35]

Since we are primarily interested in the behavior of the charge pairs which do dissociate at realistic fields, we choose
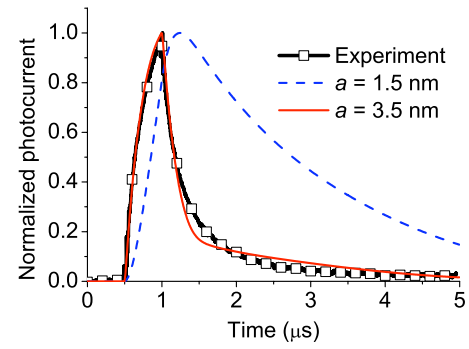
to continue to apply the Onsager–Braun approach, taking parameters which reproduce the field-dependence of our data, specifically the peak transient photocurrents seen in the 500 ns data at different applied fields. The overall charge-pair generation rate in the model is scaled [via $(G_0)_{max}$] to allow for the population of charge pairs which are not able to participate in charge separation. The ratio $k_{rec}/k_{diss}(0)$ is found to be 1.28. For the charge-pairs included in the model, $P=0.72$ at short circuit. Trapping effects are included, as before, but play a minor role on short time scales. The same parameters reproduce the steady-state current-voltage curve, as shown in Fig. 4.

The fitting performed above only allows us to determine ratio of the rate constants k_{diss} and k_{rec}, rather than their individual values. In principle, however, as discussed in our previous paper, the dynamics of charge-pair separation and recombination will influence photocurrent dynamics when they are comparable with free charge dynamics.[15] In the case of sufficiently slow charge pair dynamics there exists a time delay between the time the light is switched off and the time at which photocurrent reaches a maximum. The fact that no such delay is observed in our experiments places a lower limit on the values of k_{diss} and k_{rec}. To illustrate this, in Fig. 5 we compare photocurrent dynamics at short-circuit for two different values of initial charge-pair separation, a [and hence k_{diss} as determined by Eq. (8)] with k_{rec} chosen to give the correct value of P from Eq. (10). For a value of a $=1.5$ nm (corresponding to a charge-pair lifetime of 1 μs) there exists a time delay between turn-off and the time at which photocurrent reaches a maximum. This arises since the population of charge pairs persists after the light is turned off and some of these pairs are able to be separated and contribute to the photocurrent. However, for a value of a $=3.5$ nm corresponding to a charge-pair lifetime of 11 ns the photocurrent maximum corresponds to the time at which light is turned off, because the charge pair density decays quickly to a dark state, being unable to contribute photocurrent by dissociation after the light is turned off. Experimental limitations mean that we are unable to resolve delays below

about 50 ns, and hence from the absence of any observable delay in Fig. 5 we can place an upper bound on the charge-pair lifetime of 50 ns, corresponding to a lower bound on a of 2.8 nm. We use the value $a=2.8$ nm in Table I, corresponding to a charge-pair lifetime of 22 ns.

We note that 2.8 nm is a rather large value for a. For example, it is considerably larger than the value of a $=0.6$ nm used by Mandoc et al.[36] to describe the current-voltage characteristics of MDMO-PPV:PCNEPV all-polymer solar cells. However the MDMO-PPV:PCNEPV devices reported by Mandoc et al. have a fill factor of less than 0.25; the considerably higher fill factors seen in our devices are not consistent with small values of a. Given the fundamental limitations of the Onsager–Braun approach,[37] and the fact that we have excluded a population of rapidly recombining charge pairs from our model, it is better to consider the charge separation parameters we choose to be a useful parameterization rather than a detailed description of the underlying physics. Nevertheless, as discussed above, the photocurrent dynamics do place constraints on the time scales for charge separation and recombination.

B. Fitting of long pulse photocurrent transients

With the charge separation and transport parameters determined, we now consider the trapping and detrapping parameters. Using a trap population of $N_t=1.3\times10^{22}$ m^{-3} and trapping and detrapping rate constants of $C_t=2.5\times10^{-16}$ m^3 s^{-1} and $C_{dt}=1.0\times10^4$ s^{-1}, respectively, the numerical simulation qualitatively reproduce all of the features seen in the experimental data, Fig. 1. In particular, as highlighted in Fig. 6(b), the simulation reproduces the evolution of the transient peak with intensity and the decrease in the photocurrent tail relative to the photocurrent at 100 μs. As discussed above and elaborated in more detail below, this transient peak that occurs on a longer time scale than the transport of free charges derives from the build-up of charge in the device due to electron trapping that increases the occurrence of both geminate and bimolecular recombination. The slow photocurrent tail results from the slow detrapping of electrons after turn-off. The decrease in the area under the photocurrent tail (equivalent to the amount of charge extracted after turn-off) relative to the steady state photocurrent with increasing intensity therefore results from a finite trap population rather than charge recombination. For a situation where $n_t\ll N_t$, the ratio of the steady state trapped electron density to the free electron density is determined by the ratio $C_t N_t/C_{dt}$, and scales linearly with steady state photocurrent. For the values chosen, this corresponds to a trap depth of 0.15 eV. Since the extracted charge after turn off does not scale linearly with photocurrent,[14] it can be inferred that n_t $\sim N_t$ at the highest intensities measured which places constraints on the possible values of N_t. Figure 7(a) demonstrates the influence of the magnitude of N_t on the photocurrent tail at the highest light intensity used. C_{dt} was fixed at the value given in Table I, but C_t was varied in inverse proportion to N_t in order to maintain a constant value of $C_t N_t/C_{dt}$. For values of N_t above 8×10^{22} m^{-3} the photocurrent decay curves converge to the same trace indicating a
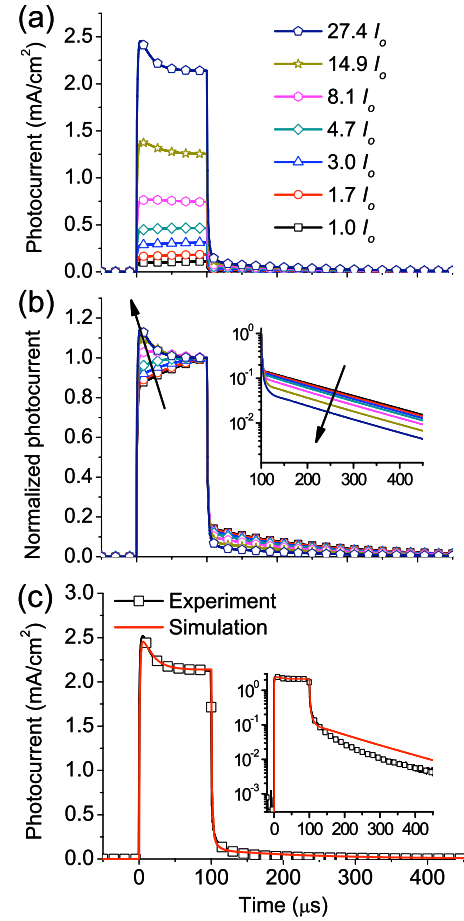

FIG. 6. (Color online) (a) Photocurrent transients calculated with different intensities when applying a 100 μs light pulse. The intensities shown are expressed as multiples of the smallest experimental intensity, I_0 $=3.3$ mW/cm^2. (b) Normalized photocurrents of (a) with the normalized falling currents on a log-linear scale in the inset. (c) Comparison to the experimental results at the highest intensity ($27.4I_0$) with the inset on a log-linear scale.

change in the trap filling regime from $n_t\sim N_t$ to $n_t\ll N_t$. Of course, the photocurrent tail is also influenced by the detrapping rate constant C_{dt}, as shown in Fig. 7(b). However, C_{dt} influences the slope of the current decay curves more than the relative magnitude, and hence we obtain an estimate of N_t from this analysis of 5×10^{21} m$^{-3}<N_t<9\times10^{22}$ m^{-3}. The lower bound of $N_t=5\times10^{21}$ m^{-3} will be discussed later in the context of Fig. 8(a). An intermediate value of N_t $=1.3\times10^{22}$ m^{-3} was chosen, which reproduces nicely the trend in relative extracted photocurrent with increasing light intensity [compare inset of Fig. 6(b) to the inset of Fig. 1(b)]. Note that as the model assumes a single trap energy, the photocurrent decay curves are linear on a logarithmic photocurrent scale. In reality, a distribution of trap energies and a distribution of transport energies will exist[38] which accounts for the different shape of the experiment photocurrent tail.

The values for C_t and C_{dt} were determined by considering the peak in the photocurrent transient after turn-on at high intensity, Fig. 8. The peak in the photocurrent is mediated by the build-up of space charge caused by the trapping of electrons in the blend. This is demonstrated in Fig. 8(a) where the influence of N_t on the photocurrent turn-on is investigated for fixed $C_t N_t$ and C_{dt}. For insufficient N_t, no peak
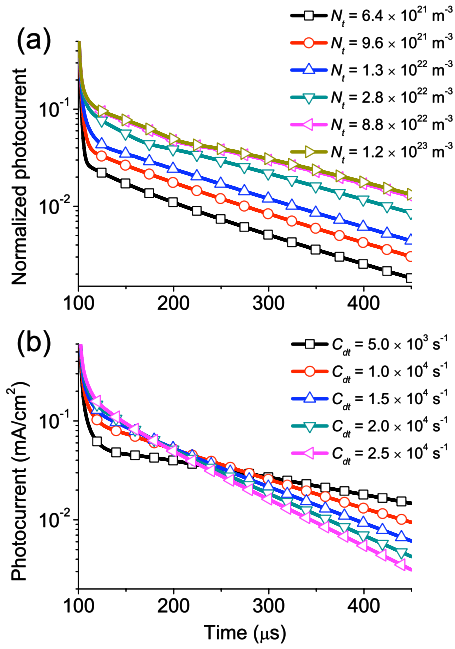
FIG. 7. (Color online) The influence of (a) the density of trap sites and (b) trapping and detrapping rate constants on falling current transients after the light ($I = 27.4 I_0$) is turned off. In (b), detrapping rate constants used are presented in the legend, and trapping rate constants are concomitantly varied to keep the same ratio of the two.

is observed as the density of traps is not enough to mediate space-charge effects. The amount by which the steady-state photocurrent transient is reduced by space charge effects [compare black (squares) curve to pink (diamonds) curve in Fig. 8(a)] is determined not only by N_t but also by the ratio C_t / C_{dt} since the trapped electron density at steady state is
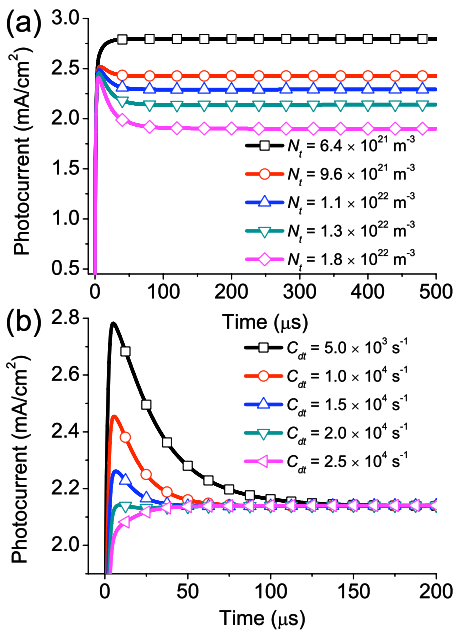

FIG. 8. (Color online) Influence of (a) the density of trap sites and (b) trapping and detrapping rate constants on photocurrent rise dynamics at the intensity ($27.4 I_0$). In part (a), $C_t N_t$ and C_{dt} are set to 3.2×10^6 and 1.0×10^4 s^{-1}, respectively. N_t is varied as shown. In part (b), N_t is set to 1.3×10^{22} m^{-3}, and C_{dt} is varied, as shown with C_t also varied from 1.2×10^{-16} to 6.1×10^{-16} m^3 s^{-1} to keep a constant ratio C_t / C_{dt}.
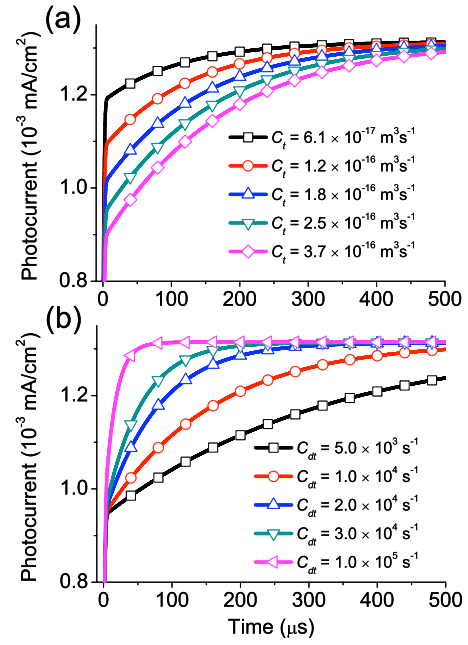

FIG. 9. (Color online) Influence of (a) trapping rate constant with $C_{dt} = 1.0 \times 10^4$ s^{-1} and (b) detrapping rate constant with $C_t = 2.5 \times 10^{-16}$ m^3 s^{-1} on photocurrent rise dynamics under weak illumination ($I = 10^{-2} I_0$).

determined by $C_t N_t / C_{dt}$. For a given value of N_t (as determined above) the ratio C_t / C_{dt} can be tuned so as to produce the required reduction in steady-state photocurrent. The ratio C_t / C_{dt} was thus determined by fitting to the highest intensity experimental curve with $(G_0)_{max}$ already independently determined from fitting to the 500 ns data. With a value for C_t / C_{dt} fixed, the absolute values of C_t and C_{dt} were determined by considering the photocurrent dynamics, Fig. 8(b). If C_t is too large, then a trapping-mediated reduction in steady state photocurrent is immediately realized without a transient peak [black (squares) curve in Fig. 8(b)]. If C_t is too small, then the time taken to reach steady-state does not match what is observed experimentally. Thus by fitting the magnitude of the photocurrent reduction *and* the dynamics [Fig. 5(c)] C_t and C_{dt} are uniquely determined.

With the value of the trapping and detrapping parameters justified, we now consider the turn-on dynamics at other light intensities. The Fig. 6(b) demonstrates that the evolution in turn-on from a slow, monotonic rise at low intensity, to a peaked curve at high intensity as observed experimentally is successfully reproduced by the model. In particular, the intensity at which the transition from monotonic to peaked rise is observed in the model matches well with what is observed experimentally (~10 to 15 mW/cm^2). Considering the influence of the trapping parameters on the turn-on dynamics at low intensity, Fig. 9, we show that in the presence of trapping, the turn-on time of the slow component is determined not by the transit time $t_{tr} = d^2 / (V \times \mu_{n(p)})$ of free charges but rather by the time taken for the trap population to equilibrate. Based on the mobilities extracted from the fit to the transient photocurrents with a 500 ns pulse, the turn-on times of free electron and hole currents are 0.5 and 5 μs, respectively. While these turn-on times are much too short to explain the full turn-on dynamics, they do account for the
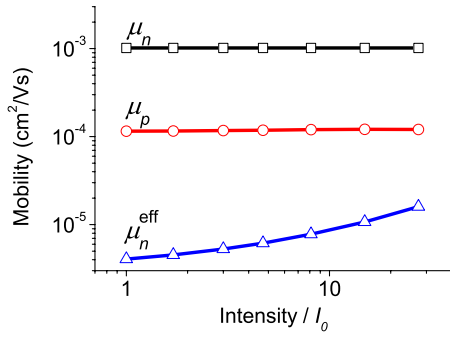
FIG. 10. (Color online) The intensity dependence of mobilities; free electron mobility ($\square$), free hole mobility, ($\bigcirc$) and effective electron mobility ($\triangle$).

fast component of the photocurrent turn-on observed experimentally. Considering the influence of the trapping and de-trapping rate constants, for a high C_t, an immediate reduction in the value to which the fast photocurrent component reaches is realized [pink (diamonds) curve in Fig. 9(a)]. The rate of the slow rise is determined solely by the detrapping process [Fig. 9(b)].

Figure 10 presents the influence of electron trapping on the effective electron mobility. From the 500 ns data, a larger free electron mobility ($\sim 10^{-3}$ cm^2/V s) than hole mobility ($\sim 10^{-4}$ cm^2/V s) was fitted. However, when electron trapping is considered, the effective electron mobility given by $\mu_n^{eff} = \mu_n n_f / n$ is much less than the free electron mobility. As the effective electron mobility is a function of the fraction of free electrons, μ_n^{eff} varies with light intensity as the equilibrium trap density varies. Figure 10 displays this trend with μ_n^{eff} varying from 4×10^{-6} to 2×10^{-5} cm^2/V s over the range of intensities used. Thus the effective electron mobility is lowered by two orders from the free electron mobility and is consistent with values measured by TOF.[20]

C. Time evolution of the internal electric field and charge recombination

A unique advantage of the time-dependent modeling approach is the ability to examine the time evolution of pro-
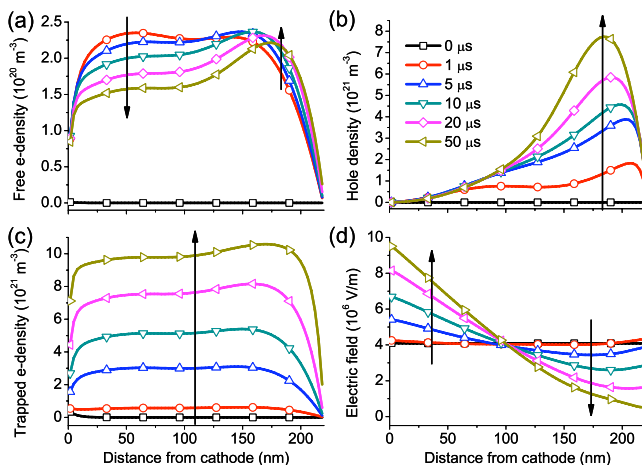

FIG. 11. (Color online) Time-evolution of (a) free electron density, (b) hole density, (c) trapped electron density, and (d) electric field for the first 50 μs at high light intensity ($I = 27.4 I_0$).

cesses inside the device. Figure 11 presents the time evolution of free and trapped electron densities, hole density and the internal electric field from 0 to 50 μs after turn-on. While increasing more slowly, the trapped electron density eventually dominates with a charge density of up to 10^{22} m^{-3} at 50 μs compared to maximum free electron and hole densities of 2×10^{21} and 8×10^{21} m^{-3}, respectively. The hole density is strongly peaked near the anode, due to the shape of optical absorption profile (Fig. 2) with more charge pairs generated near the transparent anode) and the fact that holes are collected at this electrode. Electron density in the device (both free and trapped) in contrast has a much flatter profile in general with electrons having on average to traverse the majority of the film to the cathode in order to be collected. Due to the significant build-up of trapped electrons in the device, the internal electric field becomes severely distorted with the dynamics of the evolution of the electric field distribution following the time taken for the trap population to equilibrate. As a result of the large amount of unbalanced charge near the cathode where electrons are collected, the electric field increases in this half of the device. To compensate, near the anode, the electric field decreases facilitating an increase in the hole density that further compensates the excess charge of trapped electrons here due to slower extraction of holes. The free electron density near the cathode also decreases as a result both of the increased electric field strength here and of electron trapping, resulting in a faster sweep-out of charge. Thus while free electron and hole populations would equilibrate after a few μs in the absence of trapping, the further evolution of the electric field due to trapping results in further changes in the free electron and hole densities.

The result of the distorted electric field in the device is twofold. First, due to the increased hole density (and slight increase in free electron density) near the anode, there is an increase in the likelihood of bimolecular recombination. This is shown in Fig. 12(a) where bimolecular recombination increases disproportionately near the anode even beyond the transit time of free charges due to the increased density of electrons and holes here. Second, since the charge separation process is electric-field dependent, changes in the electric field strength in the device bring about an associated change in the local free charge generation efficiency. This is shown in Fig. 12(b), where the charge dissociation rate decreases significantly near the anode. Close to the cathode there is an increase in the charge generation efficiency corresponding to the higher electric field here. However, due to the fact that the optical absorption profile is peaked close to the anode (Fig. 2) the change in the shape of the electric field distribution actually produces a net decrease in charge generation efficiency in the device. The overall reduction in charge-pair separation efficiency across the entire active layer can be shown with a single quantity P^{av}, calculated by integrating the charge generation efficiency P [Eq. (10)] with the electric field distribution and optical absorption profile via
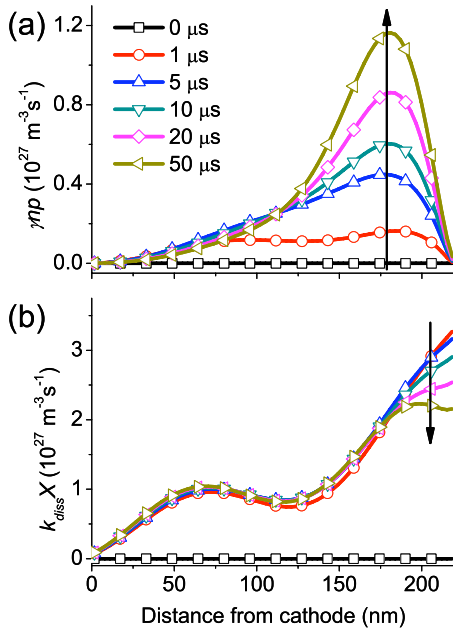
FIG. 12. (Color online) Time-evolution of (a) the bimolecular recombination rate and (b) the charge dissociation rate as a function of position in the device. We note that the rates are comparable and the charge dissociation rate decreases while the bimolecular recombination rate increases.

$$P^{\mathrm{av}} = \frac{\displaystyle\int_0^d G(z)\frac{k_{\mathrm{diss}}(z,E)}{k_{\mathrm{diss}}(z,E)+k_{\mathrm{rec}}}dz}{\displaystyle\int_0^d G(z)dz}. \tag{11}$$

Figure 13 then plots the time evolution of P^{av}, the weighted spatially averaged charge generation efficiency, demonstrating that P^{av} decreases by 20% solely as a result of the reduced charge dissociation rate due to the decreased electric field near the anode. It is also possible to calculate the net spatially averaged charge generation efficiency parameter $P^{\mathrm{av}}_{\mathrm{net}}$ defined as

$$P^{\mathrm{av}}_{\mathrm{net}} = \frac{\displaystyle\int_0^d G(z)\frac{k_{\mathrm{diss}}(z,E)X - \gamma n_f p}{k_{\mathrm{diss}}(z,E)X - \gamma n_f p + k_{\mathrm{rec}}X}dz}{\displaystyle\int_0^d G(z)dz}, \tag{12}$$

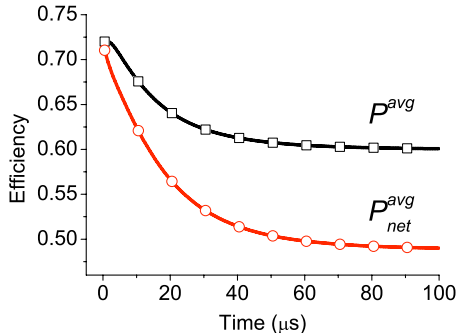which accounts also for bimolecular recombination losses and corresponds to the fraction of charge pairs that are collected as current.[15] Comparison of P^{av} and $P^{\mathrm{av}}_{\mathrm{net}}$ therefore provides a comparison of the relative importance of space-charge mediated geminate and bimolecular recombination in the system. The time evolution of these two parameters is shown in Fig. 13 with bimolecular recombination also decreasing photocurrent by around 20%. Figure 13 also shows that the difference between $P^{\mathrm{av}}_{\mathrm{net}}$ and P^{av} increases with time, indicating that bimolecular recombination gets stronger with time.[15] Therefore, suppression of charge generation and bimolecular recombination, both of which are caused by space charge effects mediated by electron trapping, play a role in producing a peak in photocurrent transients. The space charge effects and bimolecular recombination are mutually correlated, leading to a reduction in photocurrent efficiency.[39] We note, however, that we have assumed bimolecular recombination to be Langevin-like. However in other phase-separated bulk heterojunction systems bimolecular recombination has been shown to be suppressed relative to standard Langevin-type recombination due to electrons and holes being constrained in separate phases that reduces the likelihood of meeting in space and recombining.[9,10] In our effective medium approach we do not account for the possibility of a reduced bimolecular recombination rate as a result of the phase separated structure of the blend. Therefore space-charge mediated bimolecular recombination may actually be less significant than space-charge mediated geminate recombination in this system.

As an aside, we also note if hole trapping was considered instead of electron trapping, the spatially averaged charge generation efficiency would increase with time, because the dominant density of free and trapped holes would cause electric fields to increase near the anode but to decrease near the cathode after about 5 μs. In such a case of hole trapping, more charge pairs experience an increase in charge generation efficiency, so that photocurrents transients are expected to have no peak or a small dip, which is not observed in our experiment.

V. CONCLUSION

We have successfully employed a time-dependent drift-diffusion model incorporating electron trapping and electric-field dependent charge separation to describe the transient photocurrent dynamics of P3HT:F8TBT blend solar cells. The slow turn-on dynamics on the time scale of $10-100$ μs are explained by the model as resulting from the time taken for the trap population to equilibrate with the trapping and detrapping processes occurring on a longer time scale than the transport of free charges. The slow turn off dynamics with the magnitude of the long-lived photocurrent decay not scaling linearly with steady-state photocurrent is accounted for by a finite trap density with $n_t \sim N_t \cong 1.3 \times 10^{22}$ m^{-3} at light intensities approximating solar illumination. The transient peak after turn-on that is observed at high light intensities is explained by trap-mediated space-charge effects. In particular, reduction in the strength of the internal electric field near the transparent anode produces a net decrease in the free charge generation efficiency of the device that is comparable in magnitude to bimolecular recombination un-

FIG. 13. (Color online) The spatially averaged charge generation efficiency (□) and net charge generation efficiency (○) as a function of time after turn-on at high intensity ($I = 27.4 I_0$).

der these conditions assuming Langevin-type bimolecular recombination. Thus second order recombination in organic solar cells may also be mediated through space-charge enhanced geminate recombination and not solely through bimolecular recombination. Analysis of the faster photocurrent dynamics also places an upper limit on the lifetime of electron-hole pairs at 50 ns.

ACKNOWLEDGMENTS

[1] A. C. Mayer, S. R. Scully, B. E. Hardin, M. W. Rowell, and M. D. McGehee, Mater. Today **10**, 28 (2007).

[2] G. Li, V. Shrotriya, J. Huang, Y. Yao, T. Moriarty, K. Emery, and Y. Yang, Nature Mater. **4**, 864 (2005).

[3] W. Ma, C. Yang, X. Gong, K. Lee, and A. J. Heeger, Adv. Funct. Mater. **15**, 1617 (2005).

[4] S. C. Veenstra, J. Loos, and J. M. Kroon, Prog. Photovoltaics **15**, 727 (2007).

[5] B. Sun, E. Marx, and N. C. Greenham, Nano Lett. **3**, 961 (2003).

[6] V. D. Mihailetchi, L. J. A. Koster, J. C. Hummelen, and P. W. M. Blom, Phys. Rev. Lett. **93**, 216601 (2004).

[7] R. A. Marsh, C. R. McNeill, A. Abrusci, A. R. Campbell, and R. H. Friend, Nano Lett. **8**, 1393 (2008).

[8] G. Juška, K. Arlauskas, M. Viliūnas, K. Genevičius, R. Österbacka, and H. Stubb, Phys. Rev. B **62**, R16235 (2000).

[9] A. J. Mozer, G. Dennler, N. S. Sariciftci, M. Westerling, A. Pivrikas, R. Österbacka, and G. Juška, Phys. Rev. B **72**, 035217 (2005).

[10] A. Pivrikas, G. Juška, A. J. Mozer, M. Scharber, K. Arlauskas, N. S. Sariciftci, H. Stubb, and R. Österbacka, Phys. Rev. Lett. **94**, 176806 (2005).

[11] S. M. Tuladhar, D. Poplavskyy, S. A. Choulis, J. R. Durrant, D. D. C. Bradley, and J. Nelson, Adv. Funct. Mater. **15**, 1171 (2005).

[12] G. Juška, K. Arlauskas, G. Sliaužys, A. Pivrikas, A. J. Mozer, N. S. Sariciftci, M. Scharber, and R. Österbacka, Appl. Phys. Lett. **87**, 222110 (2005).

[13] T. J. Savenije, J. E. Kroeze, M. M. Wienk, J. M. Kroon, and J. M. Warman, Phys. Rev. B **69**, 155205 (2004).

[14] C. R. McNeill, I. Hwang, and N. C. Greenham, J. Appl. Phys. **106**, 024507 (2009).

[15] I. Hwang and N. C. Greenham, Nanotechnology **19**, 424012 (2008).

[16] L. J. A. Koster, E. C. P. Smits, V. D. Mihailetchi, and P. W. M. Blom, Phys. Rev. B **72**, 085205 (2005).

[17] C. R. McNeill, A. Abrusci, J. Zaumseil, R. Wilson, M. J. McKiernan, J. H. Burroughes, J. J. M. Halls, N. C. Greenham, and R. H. Friend, Appl. Phys. Lett. **90**, 193506 (2007).

[18] C. R. McNeill, J. J. M. Halls, R. Wilson, G. L. Whiting, S. Berkebile, M. G. Ramsey, R. H. Friend, and N. C. Greenham, Adv. Funct. Mater. **18**, 2309 (2008).

[19] W. F. Pasveer, J. Cottaar, C. Tanase, R. Coehoorn, P. A. Bobbert, P. W. M. Blom, D. M. de Leeuw, and M. A. J. Michels, Phys. Rev. Lett. **94**, 206601 (2005).

[20] C. R. McNeill and N. C. Greenham, Appl. Phys. Lett. **93**, 203310 (2008).

[21] D. S. Ginger and N. C. Greenham, J. Appl. Phys. **87**, 1361 (2000).

[22] S. Marianer and B. I. Shklovskii, Phys. Rev. B **46**, 13100 (1992).

[23] V. I. Arkhipov, A. V. Vannikov, G. S. Mingaleev, Yu. A. Popova, A. I. Rudenko, V. S. Saenko, and A. P. Tyutnev, J. Phys. D **17**, 1469 (1984).

[24] J. C. Scott and G. G. Malliaras, Chem. Phys. Lett. **299**, 115 (1999).

[25] J. A. Barker, C. M. Ramsdale, and N. C. Greenham, Phys. Rev. B **67**, 075205 (2003).

[26] C. L. Braun, J. Chem. Phys. **80**, 4157 (1984).

[27] H. Scher and E. W. Montroll, Phys. Rev. B **12**, 2455 (1975).

[28] L. A. A. Pettersson, L. S. Roman, and O. Inganäs, J. Appl. Phys. **86**, 487 (1999).

[29] H. Hoppe, N. S. Sariciftci, and D. Meissner, Mol. Cryst. Liq. Cryst. **385**, 113 (2002).

[30] C. M. Ramsdale and N. C. Greenham, J. Phys. D **36**, L29 (2003).

[31] C. R. McNeill, A. Abrusci, I. Hwang, M. A. Ruderer, P. Müller-Buschbaum, and N. C. Greenham, Adv. Funct. Mater. **19**, 3103 (2009).

[32] A. J. Mozer and N. S. Sariciftci, Chem. Phys. Lett. **389**, 438 (2004).

[33] T. E. Goliber and J. H. Perlstein, J. Chem. Phys. **80**, 4162 (1984).

[34] R. A. Marsh, C. Groves, and N. C. Greenham, J. Appl. Phys. **101**, 083509 (2007).

[35] C. Groves, R. A. Marsh, and N. C. Greenham, J. Chem. Phys. **129**, 114903 (2008).

[36] M. M. Mandoc, W. Veurman, L. J. A. Koster, B. de Boer, and P. W. M. Blom, Adv. Funct. Mater. **17**, 2167 (2007).

[37] H. Sano and M. Tachiya, J. Chem. Phys. **71**, 1276 (1979).

[38] M. M. Mandoc, B. de Boer, G. Paasch, and P. W. M. Blom, Phys. Rev. B **75**, 193202 (2007).

[39] N. Rappaport, O. Solomesch, and N. Tessler, J. Appl. Phys. **98**, 033714 (2005).